ADVANCED ENERGY MATERIALS
www.advenergymat.de

Origins of Abrupt Capacity Degradation in Lithium-Ion Batteries with Silicon-Based Anodes

Yoon Jeong Choi, Ji-Youn Bae, Seongsoo Park, Yeseul Kim, So Hee Kim, Hansol Lee, Jong-Seong Bae, Taeho Kim, Sunyoung Shin, Yongju Lee, Byung Mook Weon, Janghyuk Moon, and Seung-Ho Yu**

The incorporation of silicon monoxide (SiO) into graphite anodes improves the energy density of lithium-ion batteries. However, it falls short of the long-term durability of pure graphite, and research on their cycling performance remains limited. This study observes a sudden capacity decay in graphite/SiO anodes during long-term cycling at room temperature (RT) and a moderate C-rate. This decay arises from the mechanical degradation of SiO, leading to the formation of a "SiO-SEI crust" that consumes lithium ions. This phenomenon does not occur at higher temperatures or lower C-rates, implying that larger diffusion-induced stress from lithium-ion gradients at RT and 1 C accelerates SiO degradation. Furthermore, introducing a relaxation step to reduce the lithium-ion gradient mitigates this sudden capacity decay, supporting diffusion-induced stress as a critical factor in the degradation mechanism. These findings emphasize the role of diffusion-induced stress in the performance degradation of Si-based batteries and provide valuable insights for enhancing the lifespan of composite anodes.

1. Introduction

Lithium-ion batteries (LIBs) have been widely used in a variety of applications, from small portable electronics to electric vehicles (EVs) and large-scale energy storage systems.[1] As demand grows for high-capacity rechargeable batteries, particularly for EVs, interest has increased in alternatives that not only enhance the energy density of conventional LIBs, but also ensure sufficient service life.[2–5] In this context, silicon (Si) has gained attention as a promising material to surpass conventional graphite anodes due to its high theoretical capacity (3579 mAh g^{-1}) and comparable cost.[6,7] However, pure silicon undergoes significant volume expansion during the lithium alloying/dealloying process, leading to pulverization, loss of electrical contact, and excessive solid electrolyte interphase (SEI) layer formation, which ultimately shortens cell's lifespan.[8–11]

In this perspective, the anode development roadmap has evolved toward composite anodes and increasingly aims to raise the proportion of silicon-based materials relative to graphite, in order to balance high energy density with enhanced durability for industrial applications.[12,13] Among these silicon-based materials, silicon

Y. J. Choi, J.-Y. Bae, S.-H. Yu
Department of Chemical and Biological Engineering
Korea University
145 Anam-ro, Seongbuk-gu, Seoul 02841, Republic of Korea
E-mail: seunghoyu@korea.ac.kr
S. Park, J. Moon
Department of Energy Systems Engineering
Chung-Ang University
84 Heukseok-ro, Dongjak-gu, Seoul 02841, Republic of Korea
E-mail: jhmoon84@cau.ac.kr
Y. Kim, B. M. Weon
School of Advanced Materials Science and Engineering
Sungkyunkwan University
Suwon 16419, Republic of Korea
S. H. Kim, H. Lee
Advanced Analysis Center
Korea Institute of Science and Technology (KIST)
14 Gil 5 Hwarang-ro, Seongbuk-gu, Seoul 02792, Republic of Korea
J.-S. Bae
Yeongnam Regional Center
Korea Basic Science Institute (KBSI)
30 Gwahaksandan 1-ro, 60 Beon-gil, Gangseo-gu, Busan 46742, Republic of Korea
T. Kim, S. Shin, Y. Lee
Research Park
LG Energy Solution
188, Moonji-ro, Yuseong-gu, Daejeon 34122, Republic of Korea
The ORCID identification number(s) for the author(s) of this article can be found under https://doi.org/10.1002/aenm.202502143

DOI: 10.1002/aenm.202502143

monoxide (SiO) shows promise due to its reduced volume expansion compared to pure silicon, leading to improved cell lifespan and stability,[14,15] while maintaining a high theoretical capacity of ≈2600 mAh g^{-1} ($Li_{4.2-4.4}SiO$).[16] Despite significant efforts to increase the proportion of SiO, their real use remains below 5% in industry.[12] This is because anodes with high SiO content have a shorter lifespan compared to graphite-based anodes. However, to achieve maximum energy density in LIBs, increasing the SiO content in anodes is essential, while still maintaining a cycle life that meets industry standards under various operating conditions.

From this commercial standpoint, understanding the long-term cycling performance of graphite and SiO composite anodes (graphite/SiO anodes) under realistic operating conditions is essential for the advancement of high-performance LIBs. While previous studies have examined degradation mechanisms, they have often relied on nanowire silicon structures or half-cell configuration,[17–20] which do not accurately reflect the electrode architectures and limited lithium sources characteristic of full cells. Moreover, these studies typically lack evaluation of long-term cycling performance under realistic operational conditions. In half cells, lithium is continuously available from the lithium metal counter electrode, leading to fundamentally different cycling mechanisms than in full cells, where the lithium-ion source is limited to the cathode.[21,22] Consequently, investigating the cycling aging mechanisms of composite anodes within full cell configurations is essential for an accurate assessment of their long-term stability.

Furthermore, although temperature-dependent fading mechanisms of graphite anodes in LIBs are well-documented,[23–28] there is still limited understanding of how composite anodes degrade under varying temperature conditions. Insights into these fading mechanisms could inform the development of key strategies—such as electrolyte engineering and surface modifications—that improve cycling stability and energy density. Therefore, we conducted a study on composite anodes in full cell configurations across a range of realistic operating temperatures, aiming to provide a comprehensive understanding of their long-term cycling behavior.

In this study, we conducted long-term cycling performance tests with an industrial-grade full cell configuration under two temperature conditions. First, we observed a sudden capacity decay of the full cell with graphite/SiO anode at room temperature (RT,25 °C) and moderate C-rate (1 C), which did not occur at high-temperature (HT, 50 °C) or lower C-rate conditions. This sudden capacity decay was correlated with increased resistance in the SiO reaction and the loss of active SiO, with minimal contribution from changes in the cathode over cycling. Scanning electron microscopy (SEM) and computed tomography (CT) imaging revealed morphological changes in SiO during RT cycling, where the material eroded into two regions: a surface crust and bulk SiO. Energy-dispersive X-ray spectroscopy (EDS), X-ray photoelectron spectroscopy (XPS), and transmission electron microscopy (TEM) identified the crust structure as a SiO-SEI, composed of inactive SiO and electrolyte decomposition products. To the best of our knowledge, diffusion-induced stress leads to the sudden capacity decay and SiO degradation, as suggested by the formation of SiO-SEI crust under conditions where lower diffusivity results in larger lithium-ion concentration gradients. This hypothesis is further supported by simulation results and by the mitigation of capacity decay through a relaxation step, which alleviates crack propagation and SiO-SEI crust formation. These findings underscore the critical role of diffusion-induced stress in the long-term degradation of graphite/SiO full cells.

2. Results and Discussion

2.1. Sudden Capacity Decay of Composite Anode under Optimal Temperature Range

Figure 1a illustrates a schematic of the full cell configuration using a graphite/SiO (85/15 wt%) composite anode paired with an NCM622 cathode (denoted as NCM), along with a cross-sectional SEM image of the graphite/SiO anode, showing the random distribution of the two active materials. Replacing graphite with 15 wt% SiO increases the specific capacity of graphite/SiO anode by 41% compared to the graphite anode, as represented in Figure S1 (Supporting Information). Consequently, the mass loading required for the graphite/SiO anode is 34% lower than that required for graphite to achieve an N/P ratio of 1.06 with the areal capacity of NCM (≈3.3 mAh cm^{-2}), as shown in Figure 1b. This enhancement suggests that a commercial-grade composite anode system can effectively improve the full cell's energy density due to SiO's higher specific capacity. In other words, the addition of SiO reduces the anode mass loading required to achieve a specific N/P ratio.

Despite the advantages of high energy density of the composite anode, sustaining its performance over long-term cycling is influenced by various degradation factors, with temperature being particularly critical to the stability of LIBs. Common aging mechanisms of LIBs across various temperatures have been well documented in several reports.[29–34] At high temperatures, crosstalk effects and SEI instability are exacerbated, while low temperatures impede charge transfer, increasing the risk of lithium plating and internal short circuits. As a result, the optimal operating temperature range for long-term battery performance is commonly reported to be between 0 and 45 °C,[33] as this range ensures adequate ionic conductivity and minimizes undesirable side reactions. Thus, SiO-containing batteries are typically expected to exhibit inferior cycle life at elevated temperatures outside the optimal range, compared to room temperature within the generally accepted optimal range. The reduced cycle life at such elevated temperatures is primarily attributed to the combined effect of thermal interfacial instability and the intrinsic volume expansion of SiO.[35,36] To examine this expectation, an electrochemical test on full cells with graphite/SiO anodes was conducted at a 1 C/1 C (charge/discharge) under two different temperatures: room temperature (RT, 25 °C) and high temperature (HT, 50 °C), as shown in Figure 1c,d. Our experimental results revealed an unexpected, sudden capacity decay in graphite/SiO cells during long-term cycling at RT, despite it being conventionally considered an optimal operating temperature. Notably, cells cycled at RT exhibited a sharp transition ≈310 cycles, known as knee point,[37] where the rate of change in capacity loss shifts most sharply. In contrast, cells cycled at HT showed a linear capacity fade, with comparison of discharge profiles at two temperatures detailed in Figure S2 (Supporting Information). The linear capacity loss at HT continues for over 800 cycles (Figure S3,

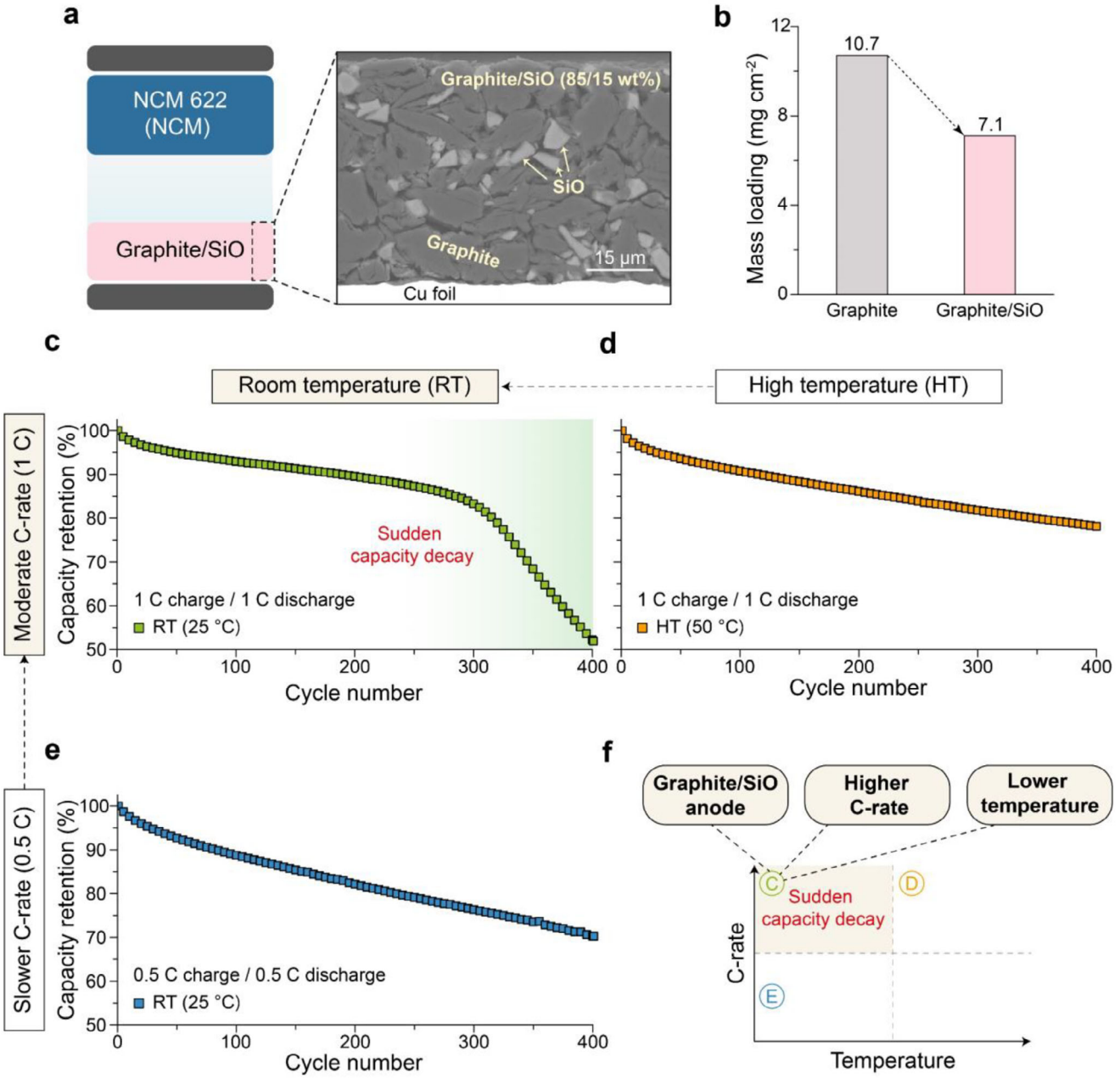

Figure 1. Full cell configuration and long-term cycling performance with the graphite/SiO anode. a) Schematic illustration of the full cell configuration and an enlarged cross-sectional SEM image of the graphite/SiO anode. b) Required mass loading of graphite and graphite/SiO anodes to achieve the same areal capacity. c–e) Discharge capacity retention of graphite/SiO anodes at c) room temperature (RT) and d) high temperature (HT) at 1 C rate and e) room temperature (RT) at 0.5 C rate. f) Schematic illustration depicting the conditions leading to the sudden capacity decay phenomenon.

Supporting Information). This finding challenges the widely accepted view that long-term battery performance improves within the optimal temperature range.

To further explore whether this rapid capacity decay is solely temperature-driven, we carried out additional electrochemical experiments across various C-rates, while maintaining the same RT conditions (see Figure 1e; Figure S4, Supporting Information). Interestingly, the sudden capacity loss observed during 1 C cycling was not present at lower C-rates (0.5 C and 0.3 C) until 400 cycles, suggesting that temperature alone may not be the primary factor driving this phenomenon. Further electrochemical testing with graphite-only electrodes under the same cycling conditions as those in Figure 1c (see Figure S5, Supporting Information) revealed that graphite cells did not experience sudden capacity decay, instead showing a linear aging during cycling. These results were confirmed through repeated cycling tests on multiple cells under 0.5 C RT, 1 C HT, and 1 C RT conditions, as presented in Figures S6–S8 (Supporting Information). In addition,

the Coulombic efficiencies and initial discharge profiles—along with the corresponding capacities from the pre-cycle, first cycle, and fifth cycle—are presented in Figures S9 and S10 (Supporting Information). These results confirm that the initial capacities were comparable across the three tested conditions. Based on these observations, Figure 1f illustrates the conditions that lead to sudden capacity decay, including higher C-rates, lower temperatures, and the use of composite anodes. This suggests that the rapid capacity decay observed at RT and moderate C-rates in SiO-containing anodes is likely governed by the kinetics of SiO, which may play a significant role in this degradation mechanism.

2.2. Degradation of Silicon Monoxide (SiO) in Composite Anode during Cycling at Room Temperature

LIBs can undergo both linear degradation and nonlinear degradation during cycling. For graphite anode, linear degradation is typically associated with side reactions such as SEI growth, whereas nonlinear degradation involves mechanisms distinct from SEI growth.[37] Therefore, the degradation observed at RT in graphite/SiO cells can be divided into two regions: a linear degradation region, where the capacity gradually declines, and a nonlinear degradation region, where the capacity begins to decrease rapidly (see Figure S11, Supporting Information). Then we plotted the cumulative discharge capacity loss every 100 cycles up to 400 cycles, based on data from the long-term cycling tests in Figure 1c,d, as shown in **Figure 2**a. Both RT and HT cycling data initially exhibited linear capacity degradation, with capacity loss at RT being less severe than at HT. Similar with the linear degradation observed in graphite, the more intense side reactions of graphite/SiO anode at HT lead to accelerated SEI growth, resulting in linear capacity fading up to 400 cycles. However, ≈300 cycles, a rapid increase in cumulative capacity loss was observed at RT, indicating the involvement of degradation mechanisms beyond SEI growth. This sudden change in degradation behavior denotes the "sudden capacity decay" of this study, followed by a rapid decline stage (see Figure S11, Supporting Information). While SEI growth primarily accounts for linear capacity loss, the onset of nonlinear capacity fade suggests the presence of an additional mechanism related to graphite/SiO anode during RT cycling.

In order to study the mechanism of sudden capacity decay, we examined the internal resistance of cells at different temperatures, as shown in Figure 2b,c. The internal resistance of each full cell cycled at different temperatures was calculated every 100 cycles up to 300 cycles, based on the instantaneous voltage drop during discharge at different depths of discharge (DoD).[38] Most internal resistance values during HT cycling remained below 10 ohms, whereas during RT cycling, they exceeded 10 ohms, as shown in Figure 2b,c. The internal resistance in cells generally decreases as temperature rises, due to the reduced activation energy of redox reactions and faster ion diffusion. Therefore, the higher internal resistance observed at RT compared to HT can be attributed to the temperature dependence of battery resistance.[39] Notably, we observed a sharp increase in internal resistance during RT cycling, especially at higher DoD, which was less pronounced during HT cycling. Our previous study showed that SiO in the composite anode is lithiated first during charging and de-lithiated last during discharging, due to the different reaction voltages of the two active materials.[36] Consequently, SiO primarily contributed to the increase in internal resistance at high DoD in the full cell at RT, highlighted in yellow in Figure 2b and detailed in Figure S12 (Supporting Information). From these results, we conclude that not only was overall internal resistance at RT consistently higher than at HT due to temperature effects, but also the increase in internal resistance was particularly pronounced in the SiO-dominant region compared to the graphite-dominant region. This indicates that the SiO is more sensitive to temperature variations, which may play a major role in the sudden capacity decay observed at RT.

Moreover, we conducted a reassembly test to identify which electrode in full cells primarily contributed to the sudden capacity decay (see Figure 2d–f). Full cells cycled for pre-cycles at RT, 200 cycles at RT, those cycled for 400 cycles at HT, and those at the decline stage at RT were disassembled. Each aged NCM and graphite/SiO electrode was then reassembled as a half-cell with lithium metal to assess their capacity delivery as active materials. Figure 2d shows the second discharge voltage profiles from half-cell tests using aged NCM obtained from full cells cycled at RT and HT. Compared to the NCM after pre-cycles (dashed line), the NCM cathodes aged under all three conditions—200 cycles at RT, decline stage at RT, and 400 cycles at HT—showed minimal capacity loss. However, the second charge voltage profiles from half-cell tests using aged graphite/SiO, which was previously cycled in a full cell paired with the cathode from Figure 2d, revealed significant capacity loss after the sudden capacity decay, which contrasts with the behavior observed after HT cycling. Notably, the voltage profile showed a shortened plateau at 0.4 V, a region (highlighted in pink) corresponding to the SiO reaction voltage. This indicates that the SiO in the composite anode degraded during the sudden capacity decay. Even though the reassembly test was conducted at a very slow C-rate to eliminate kinetic hindrances, the capacity of the graphite/SiO did not recover after the sudden capacity decay. Consequently, while NCM retained its capacity after both RT and HT cycling, the aged graphite/SiO exhibited a 28% capacity loss after the sudden capacity decay, as summarized in Figure 2f. Additionally, we conducted the reassembly test with the full cell after 527 cycles in Figure S13 (Supporting Information). The reassembled full cell with a fresh anode and aged cathode retained a stable cycle life, whereas the reassembled full cell with an aged anode and fresh cathode showed a rapid capacity retention decay. This further indicated that the sudden capacity decay was closely related to the degradation of the composite anode, not the cathode.

Figure 2g,h shows cross-sectional SEM images of the graphite/SiO anode after 200 cycles and after sudden capacity decay at RT, as well as after 300 cycles at HT. After the sudden capacity decay, damaged SiO particles in the graphite/SiO anode were observed, which had not been seen until 200 cycles at RT (see Figure 2g). In contrast, the graphite particles showed minimal change after 300 cycles at RT, as shown in Figure S14 (Supporting Information). Furthermore, no such damaged SiO particles were observed during HT cycling, as shown in Figure 2h. The comparison of these cross-sectional SEM images after RT and HT cycling directly confirmed a distinct difference in the mechanical degradation of SiO within the graphite/SiO anode under the two temperature conditions. Consistent with previous

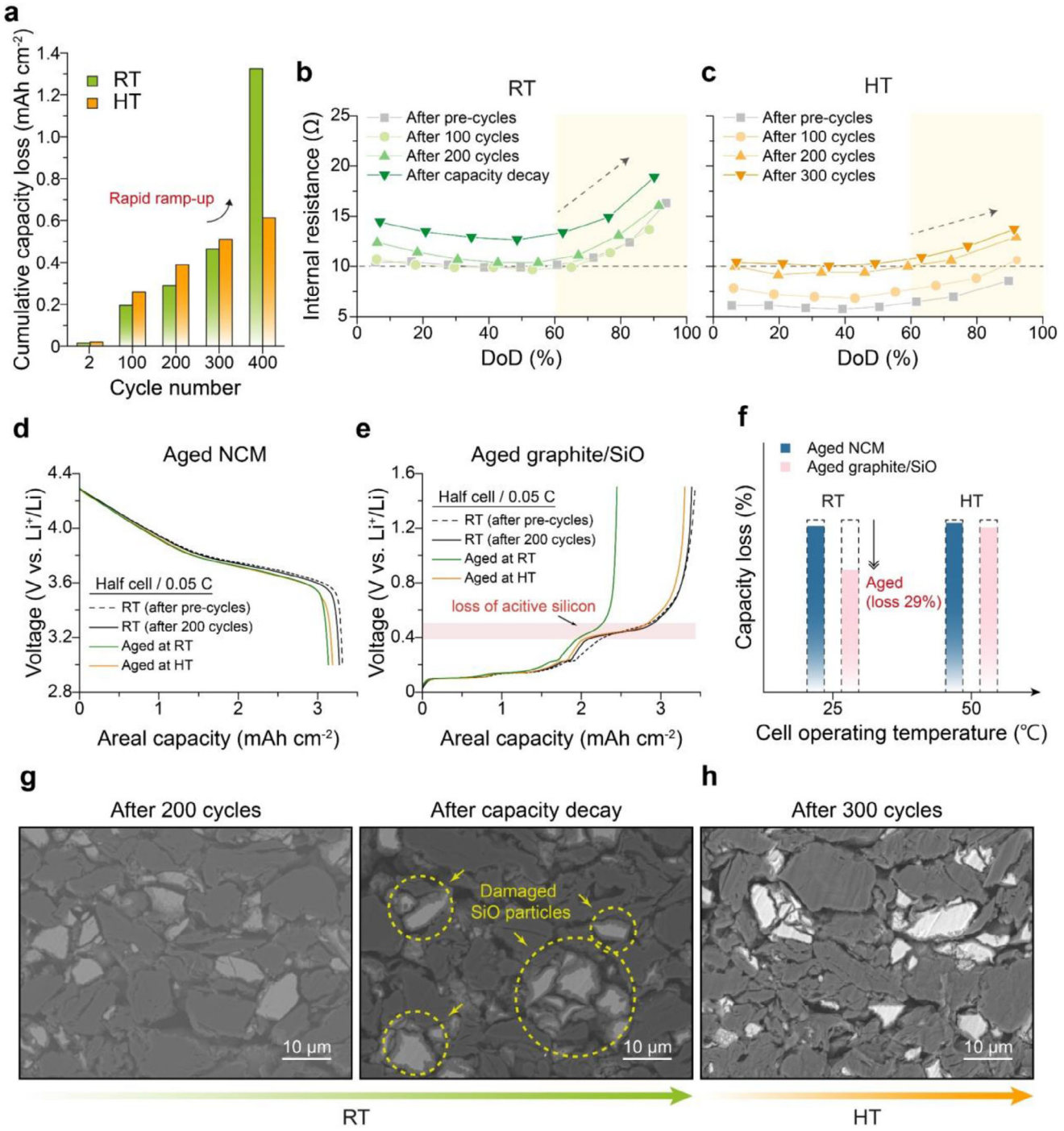

Figure 2. Electrochemical and post-mortem SEM analysis at two different temperatures. a) Cumulative discharge capacity loss of a full cell with graphite/SiO anode, obtained by summing capacity loss at each cycle and presented at every 100 cycles, at RT (green) and HT (orange). b–c) Internal resistance of a full cell with graphite/SiO anode, measured every 100 cycles, at b) RT and c) HT. d–e) Reassembly test results: d) half-cell discharge profiles of aged NCM622 and e) half-cell charge profiles of aged graphite/SiO collected from full cell aged for a specific number of cycles at two different temperatures. Voltage profiles after three pre-cycles are shown as dashed lines. f) Comparisons of the relative capacity loss (%) of the anode and cathode at RT and HT, referenced to aged electrodes from a full cell cycled for 200 cycles at RT, based on data from Figure 2d,e. g,h) Cross-sectional SEM images of the graphite/SiO anode collected from a full cell: g) after 200 cycles and sudden capacity decay at RT and h) after 300 cycles at HT.

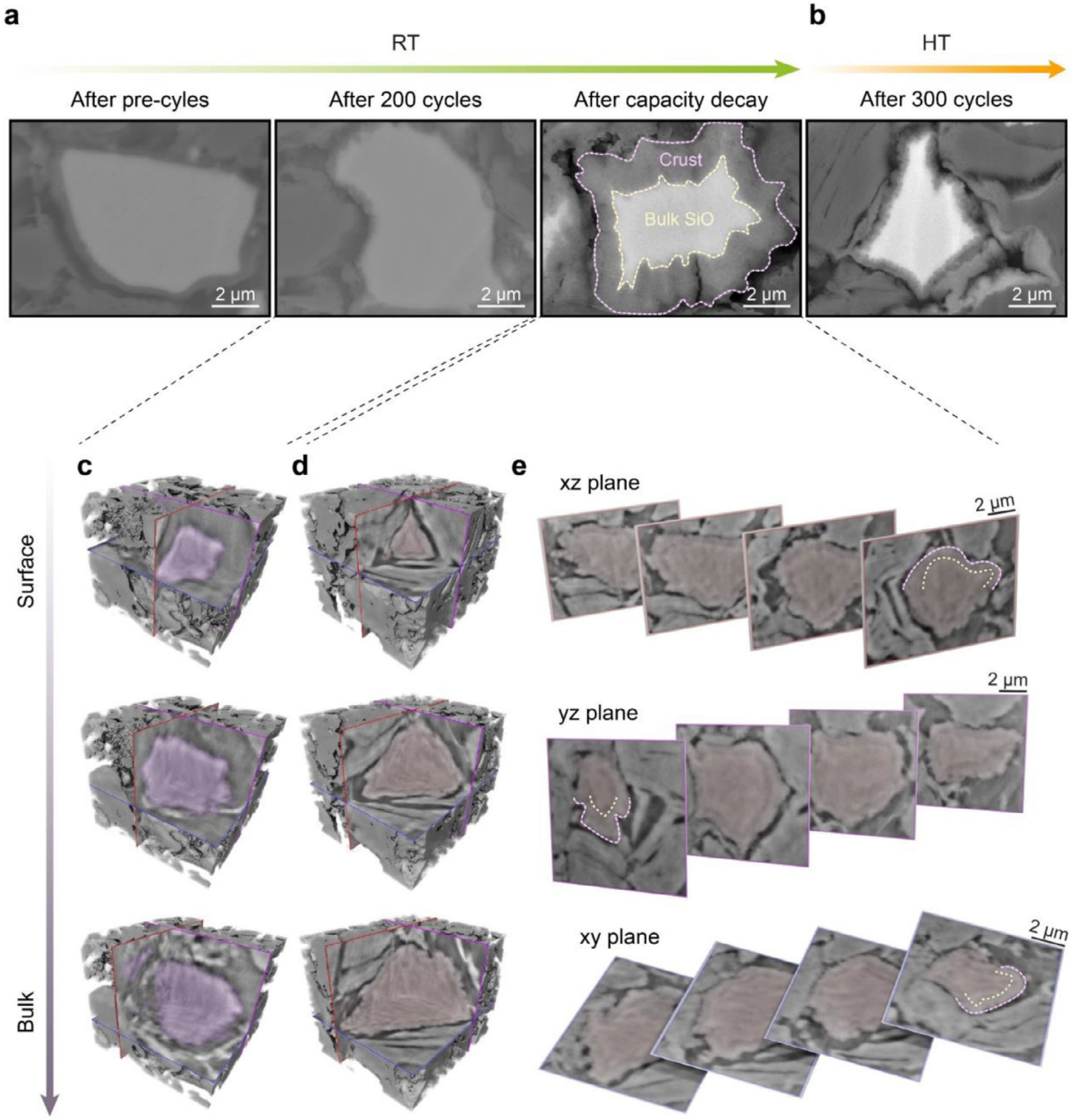

Figure 3. Morphological evolution of SiO particles by SEM and X-ray computed tomography (CT). a,b) Cross-sectional SEM images of graphite/SiO anode a) after pre-cycles, 200 cycles and sudden capacity decay at RT and b) after 300 cycles at HT. c–e) X-ray CT 3D images of the graphite/SiO anode: c) after 200 cycles at RT and d) sudden capacity decay at RT and e) corresponding sliced CT images in the direction of three plane (xz plane: red, yz plane: purple, and xy plane: blue) for (d).

observations from electrochemical tests, this finding suggests that the sudden capacity decay observed only at RT is likely related to the SiO damage.

2.3. Uniform Crust Formation on the Surface of SiO Particles

To further examine this damage, **Figure** 3a,b shows magnified SEM images of individual SiO particles after cycling. The SiO particles after the sudden capacity decay show distinct surface damage, including the formation of a crust layer over 1 μm thick, which is not observed in particles before the decay at RT or those cycled at HT, as indicated by the dashed line. This crust layer, characterized by its clear contrast with the bulk SiO region, maintains a similar thickness across particles in similar size, regardless of their position within the electrode (see Figure S15, Supporting Information). Since this crust was not observed after 300 cycles at HT, these observations indicate that crust formation is

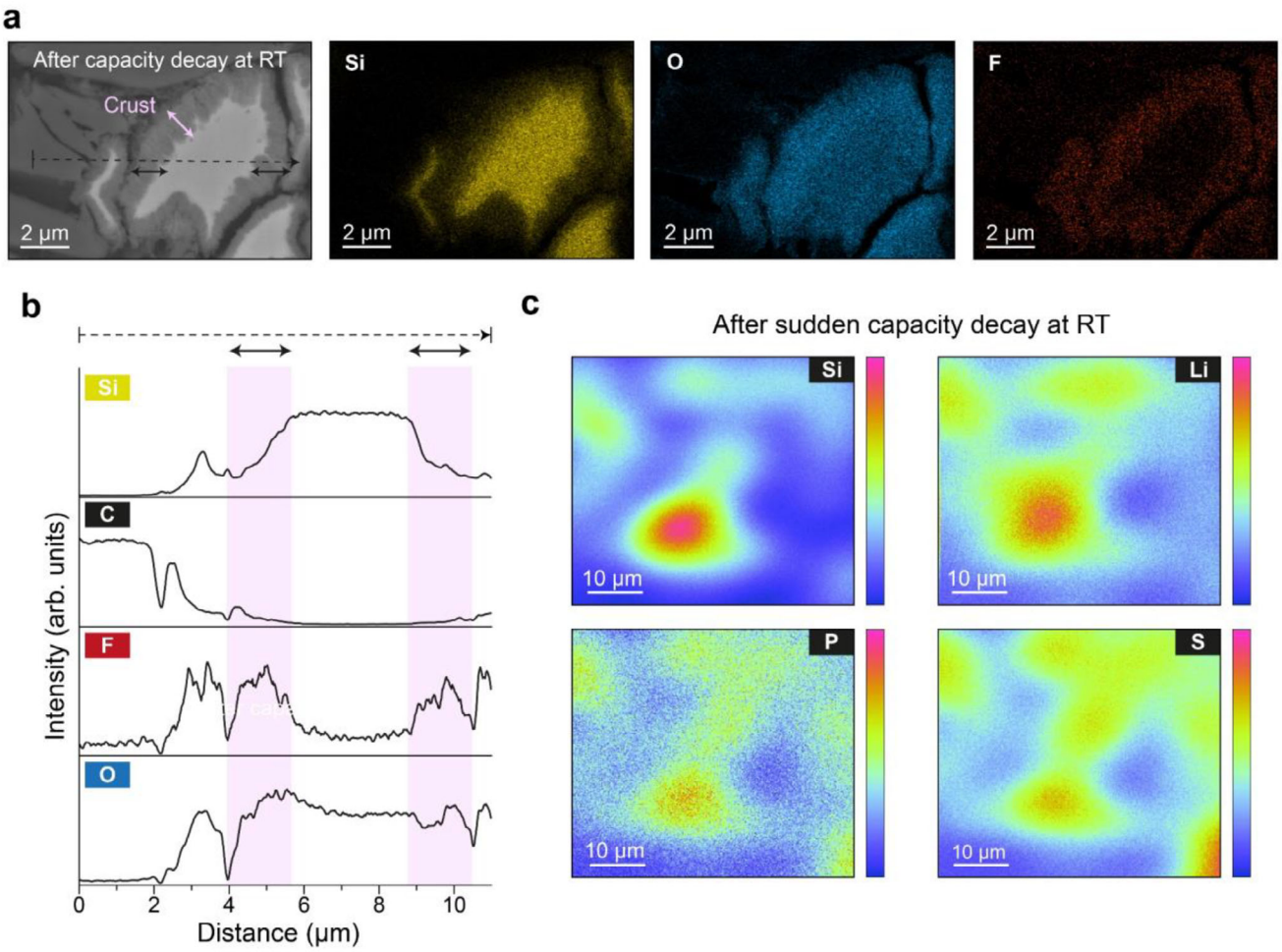

Figure 4. Composition of SiO after sudden capacity decay. a,b) Cross-sectional SEM images and a) corresponding EDS elemental maps of graphite/SiO anode after the sudden capacity decay b) corresponding line scan profiles of four elements: silicon (Si), carbon (C), fluorine (F), and oxygen (O). c) D-SIMS mapping of the graphite/SiO anode after the sudden capacity decay, showing the distribution of four elements: silicon (Si), lithium (Li), phosphorous (P), and sulfur (S).

specific to the sudden capacity decay. Additionally, we observed the evolution of the crust at sudden capacity decay region (see Figure S16, Supporting Information). Just before the capacity decay, crust formation on SiO begins, and this crust gradually grows throughout RT cycling. Thus, morphological changes in SiO are minimal before the sudden capacity decay; however, once the cell enters this region, SiO begins to degrade, with the crust growing beyond 1 μm on the surface during RT cycling.

X-ray computed tomography (CT) analysis was conducted to further explore the 3D morphology of the crust. By rotating the particles and collecting multiple X-ray projections, a 3D image of the particles was reconstructed.[40] The 3D cube images in Figure 3c,d present the results for particles cycled for 200 cycles at RT and those cycled beyond the sudden capacity decay, respectively. The 3D cube is sliced in the direction of three planes colored red, purple, and blue, showing the internal structure of SiO by processing the structure from the outer to the inner part of the cube. After 200 cycles at RT, no crust is visible in any region. In contrast, after the sudden capacity decay, the difference in contrast between the crust and the bulk SiO clearly indicates that a uniform crust has formed across the entire surface of the particle. Moreover, as shown in Figure 3e, images scanned along the xz, yz, and xy planes confirm that the crust is detected near the surface of the particle and exhibits a relatively consistent thickness, with this uniformity visualized more clearly in Videos S1 and S2 (Supporting Information).

2.4. Composition of Micrometer SiO-SEI Crust

We conducted SEM-EDS analysis to examine the composition of the crust on SiO particles. **Figure** 4a shows the cross-sectional images and corresponding EDS elemental maps of the graphite/SiO anode after sudden capacity decay. As indicated by the elemental maps, the crust on the SiO particles is composed of silicon (Si), oxygen (O), and fluorine (F), with fluorine being the only element sourced from the electrolyte in our study. Unlike the bulk of the SiO particle, the intensity of fluorine is concentrated in the crust, while the intensity of Si decreases. Figure 4b presents the elemental line scan profiles of the SiO particles in Figure 4a.

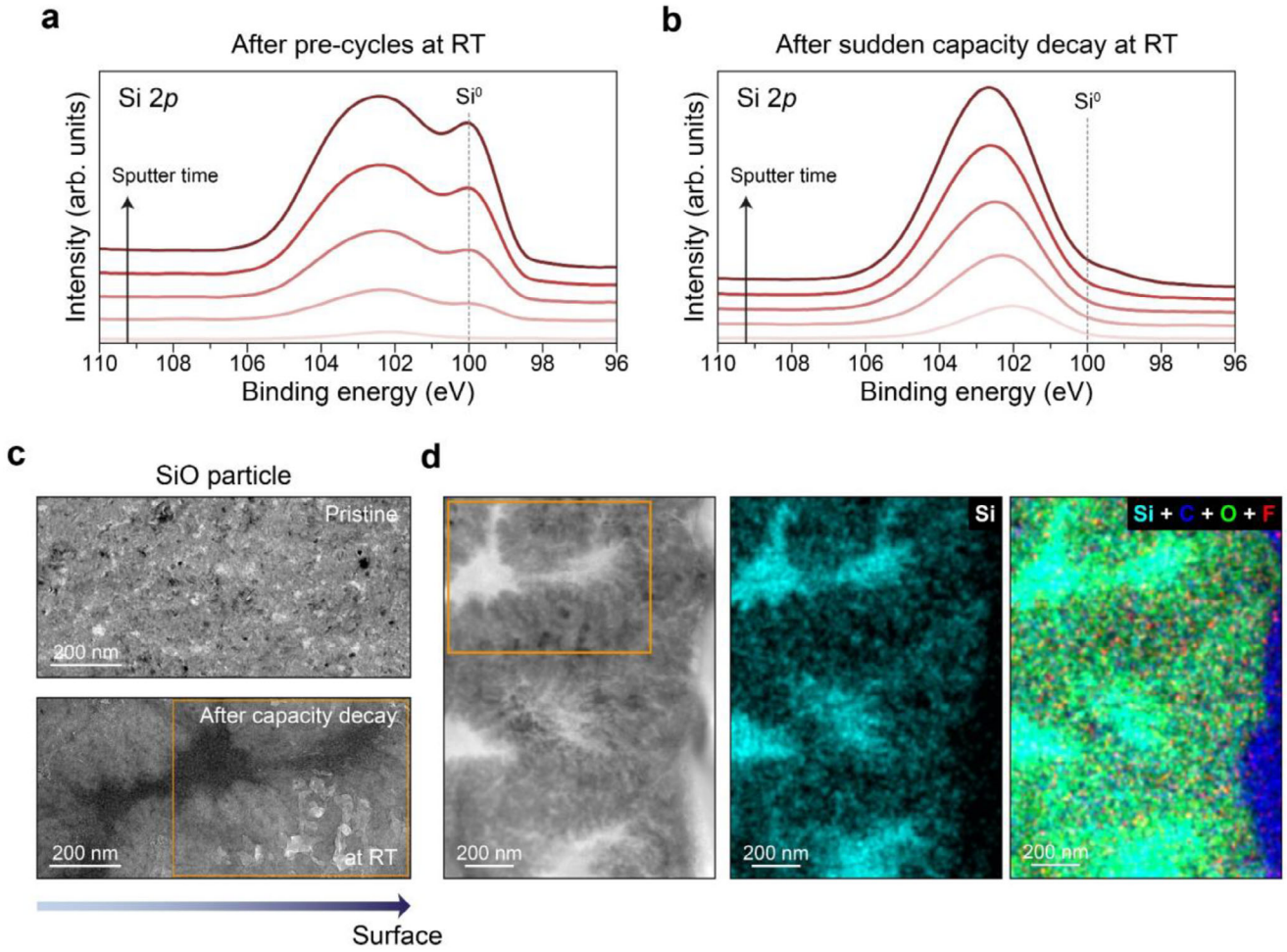

Figure 5. Composition of micrometer SiO-SEI crust a,b) XPS depth profiling of Si 2*p* spectra of the graphite/SiO anode collected from full cell a) after pre-cycles and b) after sudden capacity decay. The profiles were plotted every 500 s up to 2000 s by Ar^+ sputtering. c) Comparison of TEM images in pristine SiO and SiO after sudden capacity decay. d) HADDF-STEM image and corresponding EDS maps of SiO particle after sudden capacity decay.

Along the black dashed line, fluorine intensity increased significantly in crust on SiO, as indicated by black arrows, while carbon (C) and oxygen also show a slight increase in the surface of SiO particle. The presence of carbon, oxygen, and fluorine—components commonly found in the SEI layer[41,42] (e.g., Li_2O, Li_2CO_3, LiF, etc.)—suggests that this crust is largely composed of SEI layer, attributed to electrolyte decomposition during cycling. Similar results were observed from the dynamic secondary ion mass spectroscopy (D-SIMS) analysis of the graphite/SiO anode after the sudden capacity decay (see Figure 4c). In this top-view images from D-SIMS, regions with higher silicon intensity correspond to the locations of SiO particles within the composite anode. Lithium (Li), phosphorus (P), and sulfur (S) were detected around SiO particles, whereas their intensity was negligible around graphite particles in the graphite/SiO anode. Since lithium, phosphorus, and sulfur are also the electrolyte components in this study, the significant detection of these elements suggests that crust formation was influenced by electrolyte side reactions. Given the analysis of de-lithiated graphite/SiO anode, lithium near SiO results from SEI, trapped lithium ions,[43] and Li_xSiO_y,[44] indicating the consumption of reversible lithium during cycling. Consequently, the surface of SiO particles degraded into SiO-SEI crust over 1 μm, consuming both electrolyte and limited lithium sources.

Furthermore, we compared the X-ray photon spectroscopy (XPS) depth profiles of the pre-cycled graphite/SiO electrode with the graphite/SiO electrode after the sudden capacity decay, as shown in **Figure 5**a,b. SiO is typically composed of Si domains and SiO_2 domains, where the Si domains participate in lithiation/delithiation reactions, while the SiO_2 domains function as a structural matrix. Accordingly, the Si^0 peak observed at 98–99 eV in the XPS spectra[45,46] corresponds to the Si domains within the SiO. After pre-cycling, the presence of the Si^0 peak up to a depth of ≈200 nm indicates that the SiO particles remain intact. However, after RT cycling, the Si^0 peak disappears due to the oxidation of the Si domains in SiO, likely caused by side reactions between SiO and the electrolyte. Additionally, the reduced Si^0 peak after the sudden capacity decay aligns with the reassembly test results in Figure 2e, indicating that SiO in the crust is no longer functional as an active material, literally turning into "inactive" SiO during RT cycling. Based on these findings regarding chemical changes of composition and active material loss after the sudden

capacity decay, we conclude that only RT cycling leads to the formation of a micrometer-scale crust structure.

Transmission electron microscopy (TEM) and high-angle annular dark-field scanning transmission electron microscopy (HAADF-STEM) were employed to analyze the spatial distribution of components within the SiO-SEI crust. As shown in TEM analysis (see Figure 5c), the SiO surface, initially exhibiting a homogeneous structure under pristine conditions, displayed noticeable density variations after cycling, indicating a transition to a heterogeneous structure. HAADF-STEM imaging and EDS mapping (see Figure 5d) further clarified the composition and spatial organization within the heterogeneous structure of the crust. The denser regions correspond to elongated SiO domains, primarily connected to the bulk SiO, with a smaller fraction existing as isolated clusters (see Figure S17, Supporting Information). In contrast, more porous regions were identified as SEI components, including carbon, oxygen, and fluorine, formed through electrolyte decomposition (see Figure S18, Supporting Information), consistent with the composition previously characterized in Figure 4a. These findings suggest that partial fractures of the SiO surface during cycling produced excessive SEI and resulted in the formation of porous regions composed of SEI and inactive SiO. However, certain surface areas remained unfractured, continuing to exist as active SiO domains connected to the bulk.

By integrating structural and compositional analyses across various observations, the SiO-SEI crust was found to consist of two primary regions: inactive areas dominated by SEI and inactive SiO, which form the majority of the crust, and smaller regions of active SiO domains. Meanwhile, the inner bulk SiO remained intact, preserving its original structure. This surface transition indicates that surface fragmentation and the associated formation of excessive SEI are the primary mechanisms driving the degradation of SiO particles during cycling, ultimately leading to the development of a micrometer-scale crust and capacity fade in SiO-containing cells.

2.5. Origins of Abrupt Capacity Degradation: Focus on Diffusion-Induced Stress in SiO

So far, we found that SiO-containing cells cycled at RT undergo sudden capacity decay, which is related to the formation of a SiO-SEI crust structure. The remaining inquiry is why this structural transition during the sudden capacity decay occurs specifically on the outer surface of SiO and under specific conditions (RT and over moderate C-rate). First, we investigated the influence of the SEI formed during cycling. The characteristics of the SEI at RT may differ from those at high temperature (HT) due to thermal decomposition of organic components and enhanced formation of inorganic species.[36] To examine this, we compared XPS spectra (C 1*s*, O 1*s*, F 1*s*, Li 1*s*, and Si 2*p*) obtained from graphite/SiO anodes after pre-cycling at RT and HT (Figure S19, Supporting Information), as well as after extended cycling (300 cycles at RT and 320 cycles at HT, Figure S20, Supporting Information). No significant differences were observed in the overall SEI composition, except that the SEI formed at HT after 320 cycles exhibited higher signals from inorganic species and weaker signals from organic components. To further evaluate whether SEI characteristics influence the occurrence of sudden capacity decay, we conducted an additional cycling test in which the full cell was initially cycled at 1 C and HT for 100 cycles, followed by continued cycling at RT. As shown in Figure S21 (Supporting Information), the cell still exhibited a sudden capacity decay around the 400th cycle, which occurred after ≈300 cycles at RT following the initial 100 cycles at HT. This coincides with the cycle number at which sudden capacity decay occurs in cells cycled entirely at RT. These findings suggest that, even with sufficient SEI formation at HT, the subsequent capacity degradation at RT occurs regardless of SEI properties. Therefore, SEI characteristics are not the primary cause of the sudden capacity decay.

To determine whether the degradation behavior is associated with changes in electrode voltage profiles, we performed three-electrode full cell measurements at two temperatures (RT and HT) and two C-rates (0.2 and 1 C), as shown in Figure S22 (Supporting Information). The measured anode voltage ranges remained largely consistent across all conditions. In addition, the discharge areal capacities were similar between RT and HT until the onset of sudden capacity decay at RT (Figures S6 and S7, Supporting Information). These results suggest that the SiO component in the anode contributed similarly to the overall capacity under both temperature conditions prior to the degradation. Therefore, we conclude that neither the anode voltage range nor the utilization of SiO is affected by temperature or C-rate.

Given that the electrochemical window and SEI characteristics appear comparable across conditions, and that this phenomenon persists irrespective of binder type (Figure S23, Supporting Information), we next considered the possibility that lithium-ion diffusion in SiO, which is affected by temperature and C-rate, might be responsible for the observed degradation behavior. SiO is known to exhibit relatively low Li^+ diffusivity compared to other anode materials (Figure S24, Supporting Information), which makes it more susceptible to diffusion-related limitations. To analyze how variations in diffusivity induce local concentration variation and stress generation within the SiO material, the finite element analysis was conducted, as shown in **Figure 6**. When the diffusivity of Li^+ in SiO is relatively high, indicating the Li^+ moves quickly within the SiO particles, the concentration gradient from the surface to the center of the particle is not significantly observed during the lithiation and delithiation process. In detail, the concentration maximum difference was only 0.167 between center and surface of SiO, as shown in Figure 6a and Figure S25 (Supporting Information). In contrast, when the Li^+ diffusivity within the SiO particle slows down, this lower diffusivity of Li^+ leads to increased concentration non-uniformity. The maximum concentration difference reaches 0.809, which is 4.84 times higher than that observed under fast diffusion conditions, as shown in Figure 6d, Figure S25, and Video S3 (Supporting Information). As it is known that the diffusion of Li^+ into an active material is accompanied by a volume change of it, this uneven distribution of Li^+ concentration in a particle will form lithium-rich phase and lithium-poor phase and induce mismatch strain at the interface between phases.[47,48] This allows us to deduce that the steeper lithium gradient within SiO particles, caused by kinetic limitations (e.g., lower temperature and faster C-rate), can generate significant diffusion-induced stress and trigger the formation of defects at interface.[49,50] To explore stress distribution within particle induced by concentration variation according to the diffusivity of SiO, the normalized von Mises stress ($\sigma_{mises}/\sigma_{yield}$),

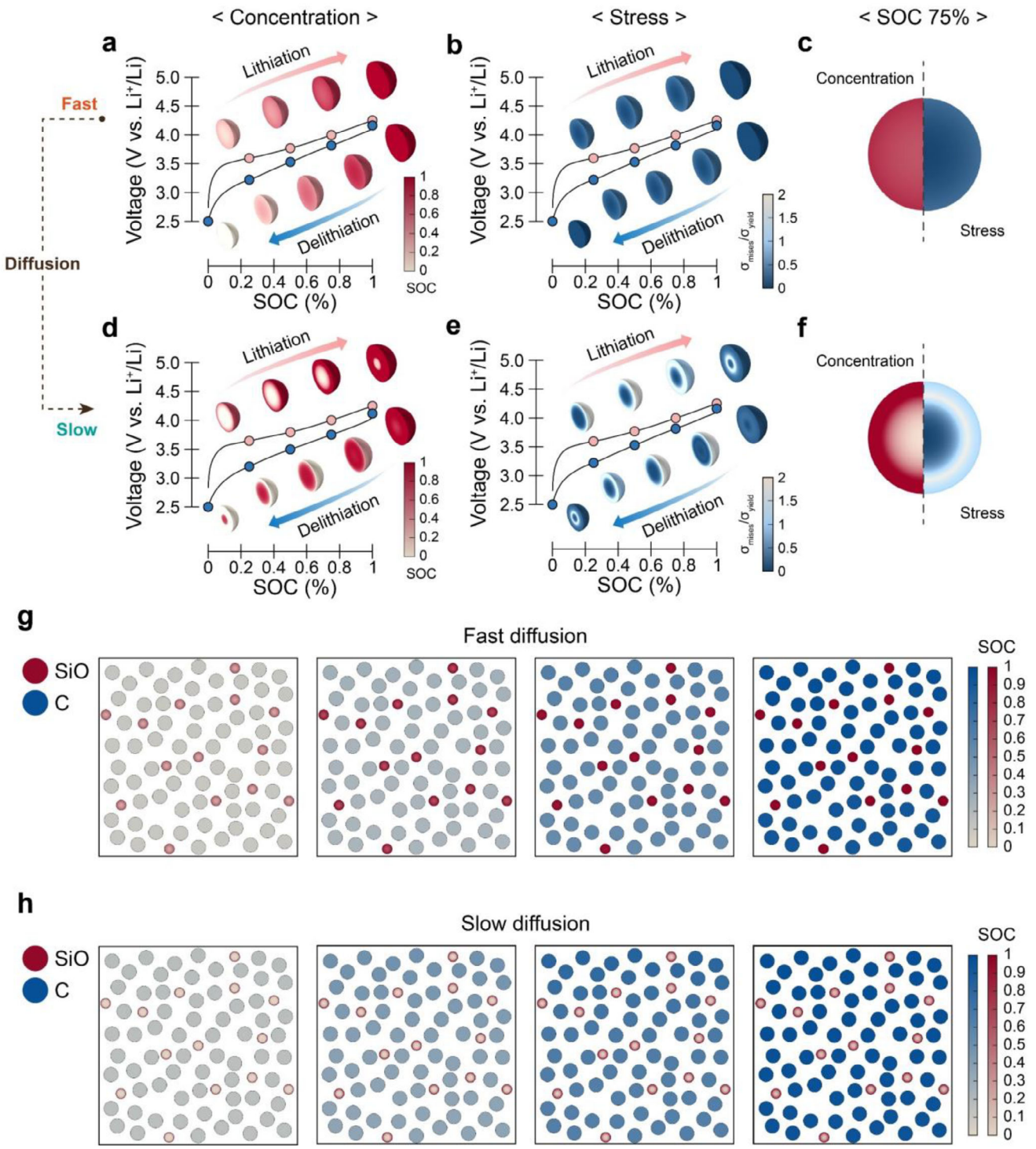

Figure 6. Simulation results showing the distribution of Li^+ concentration and stress in the SiO particle during cycling. a,b) Cycling process (charging – resting – discharging) of SiO particle under fast diffusion ($D_3 = 10^{-10.5}$ cm^2 s^{-1}) and 1 C conditions: a) concentration distribution, b) stress distribution. c) Enlarged SiO particle at 75% SOC under D_3. d,e) Cycling process (charging – resting – discharging) of SiO particle under slow diffusion ($D_1 = 10^{-11.5} cm^2$ s^{-1}) d) concentration distribution, e) stress distribution. f) Enlarged SiO particle at 75% SOC under D_1. g,h) The Li^+ concentration within graphite and SiO particles during charge process in a graphite/SiO anode. g) under fast diffusion, h) under slow diffusion.

which predominantly occurs at the particle surface, was analyzed (see Figure 6b). The results show that the low concentration variation due to the high diffusivity of Li^+ within SiO particles maintained the normalized von Mises stress at a low level of ≈0.3 throughout cycling. However, under slow diffusion conditions, the low mobility of Li^+ leads to its accumulation at the particle surface, resulting in the local volumetric expansion difference compared to the center of the particle. This local volumetric expansion at the surface leads initial development of stress at the surface of the SiO particle during the early stages of lithiation. As lithiation progresses, significant stress differences arise within the particle, particularly at the interface between regions with varying Li accumulation. This results in a pronounced stress gradient, forming a characteristic ring-like stress distribution, as shown in Figure 6e, Figures S25–28, and Video S4 (Supporting Information). The normalized von Mises stress originated from the surface is 7.38 times higher than that of SiO in faster diffusion. Figure 6c,f presents magnified SiO particles at 75% state of charge (SOC), showing both concentration and stress distribution within the particle. Note that low Li^+ diffusivity in SiO particles, which is affected by the operating temperature, triggers increased concentration non-uniformity and leads to greater stress development at the particle surface. In contrast, high Li^+ diffusivity alleviates concentration non-uniformity, thereby mitigating stress evolution. This trend was similarly observed in the graphite/SiO composite electrode, as shown in Figure 6g,h, and in Videos S5 and S6 (Supporting Information). Therefore, we concluded that during HT cycling at 1 C, SiO particles in the composite anode are fully lithiated without significant concentration gradients, minimizing diffusion-induced stress at the SiO surface; during RT cycling at 1 C, the SiO particles experience higher surface stress, and repeated charge-discharge cycles cause the surface of SiO particles to maintain elevated stress levels compared to HT cycling. These continued higher diffusion-induced stresses at the SiO surface result in particle crack from the surface, additional formation of SEI at new interface, and finally it interrupts the diffusion of Li^+ in SiO, making parasitic cycles during sudden capacity decay. This makes the sudden capacity decay observed experimentally.

To further investigate whether the sudden capacity decay is consistently associated with diffusion-limited kinetics, we extended our experiments to more extreme cycling environments, including lower temperatures (5 and 15 °C) and higher C-rate (2 C). Sudden capacity decay was also observed under these conditions—specifically, at both lower temperatures and at a C-rate of 2 C—as shown in Figure S29 (Supporting Information). Notably, the onset of capacity decay occurred earlier as the temperature decreased. These results reinforce the notion that kinetically constrained environments—arising from either low temperatures or high current densities—are critical in triggering the sudden capacity decay observed in our study.

2.6. Mitigation of Sudden Capacity Decay by Stress Relaxation of SiO

To investigate the influence of stress relaxation on SiO surface behavior under consistent applied stress, we maintained identical C-rate during charging and discharging while varying the rest duration. The rest duration was extended from 20 min to 1 h and 20 min, ensuring a 1 C cycling rate to preserve consistent stress (see **Figure** 7a). Simulations revealed that 20-min rest was insufficient for stress relaxation, as the normalized von Mises stress decreased only slightly from 0.105 to 0.086 (see Figure 7b) In contrast, the 1 h-and-20 min rest period effectively alleviated surface stress, nearly eliminating it entirely (see Figure 7c,d). Under the extended rest condition, stable cycling was achieved at RT and 1 C, conditions where sudden capacity decay typically occurs with a 20-min rest duration (see Figure 7e). SEM imaging and EDS mapping further confirmed reduced SiO particle damage, the absence of crust formation, and decreased electrolyte decomposition compared to standard cycling conditions (see Figure 7f).

These results demonstrate that not only the magnitude of stress during cycling but also the persistence of stress is imperative in SiO surface fragmentation and cycling stability. Our investigation provides direct evidence that prolonged and intense diffusion-induced stress fractures the SiO surface, leading to the formation of the SiO-SEI crust. This study offers insights into the mechanisms that drive sudden capacity decay in SiO-containing cells.

2.7. Discussion

In this study, we combined experimental and computational techniques to investigate the sudden capacity fading mechanism in full cells with graphite/SiO anode. Based on our findings, we propose a comprehensive mechanism for the long-term cycling behavior of graphite/SiO anodes, illustrated in **Figure** 8. This figure outlines the transitions of SiO particles under different cycling conditions. We categorized aging behaviors into two types: Type 1 (non-linear aging) and Type 2 (linear aging) (see Figure 8a). Type 1 aging is characterized by a gradual decline in capacity followed by a sudden capacity decay near the end of life, while Type 2 aging shows a steady, linear capacity loss throughout the battery's lifespan.

Our long-term cycling tests under various conditions revealed that graphite/SiO anode full cells experience sudden capacity decay at RT and a 1 C cycling rate (Figure 8b). Under these conditions, where the solid-state diffusion of Li^+ in SiO is relatively lower, the limited movement of lithium ions creates a steeper concentration gradient, and this concentration non-uniformity induces stress at its interface. Initially, this stress is insufficient to cause plastic fracture, which typically occurs in larger silicon-based materials during lithiation. However, as cycling progresses, the continued higher stress on SiO surface induces crack formation and propagation of preexisting cracks on the surface of SiO, resulting in fatigue failure of the active material. Once this mechanical damage occurs at the surface of SiO, electrolyte decomposition takes place in these damaged regions, depleting reversible Li^+. The resulting SEI further impedes lithium diffusion within SiO. This accelerates degradation and triggers sudden capacity decay. Various analysis after the sudden capacity decay revealed a transition of the pristine SiO surface into a SiO-SEI crust, with two distinct features: 1) active SiO domains still connected to bulk SiO and 2) inactive SiO-SEI regions formed through oxidation of active Si and additional SEI formation. This unique structure was observed only at RT and 1 C cycling

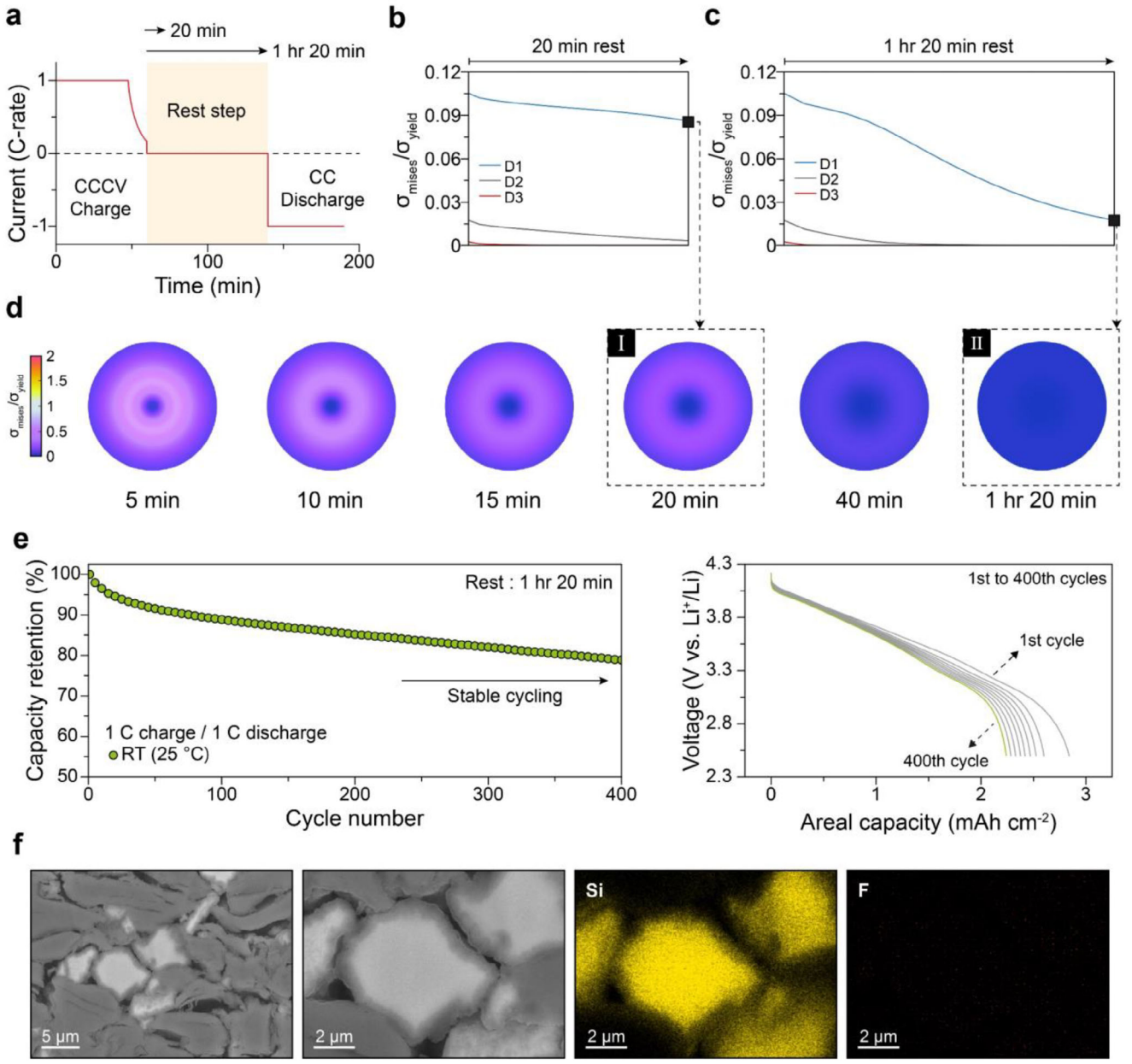

Figure 7. Particle stress alleviation by extending rest step duration. a) Cycling protocol at a 1 C rate with extended 1-h-20-min rest step. b,c) Simulation results showing the normalized von Mises stress ($\sigma_{mises}/\sigma_{yield}$) occurring at the surface during different rest time: b) 20-min rest and c) extended 1-h-20-min rest step under different diffusivity ($D_1 = 10^{-11.5}$ cm^2 s^{-1}, $D_2 = 10^{-11}$ cm^2 s^{-1}, $D_3 = 10^{-10.5}$ cm^2 s^{-1}). d) Normalized von Mises stress distribution of SiO during 1-h-20-min rest. e) Capacity retention of the graphite/SiO anode at RT with extended rest step and corresponding discharge profiles. f) Cross-sectional SEM images and corresponding EDS elemental maps of the graphite/SiO anode collected from a full cell after 320 cycles with extended rest step at RT.

conditions, suggesting that the rapid consumption of reversible Li^+ and the formation of the SiO-SEI crust are key contributors to sudden capacity decay.

Figure 8c illustrates the effect of an extended rest step in alleviating stress on SiO. Although low diffusion at RT and 1 C generates stress, this stress is mitigated by introducing a rest period of 1 h and 20 min in each cycle. The rest step relaxes the steep lithium concentration gradient, preventing the formation of the SiO-SEI crust and enabling the cell to follow a linear aging trajectory. Therefore, the stress-driven transition of SiO is mitigated by adding a rest step, which induces stress alleviation during cycling, further demonstrating that this sudden capacity decay is caused by the persistent stress on the SiO surface.

Figure 8d highlights the absence of the SiO-SEI crust structure under high-temperature or low C-rate conditions, attributed to the uniform lithium concentration. At higher temperatures, the solid-state diffusivity of Li^+ is improved, ensuring a uniform concentration within the SiO and minimizing stress at its

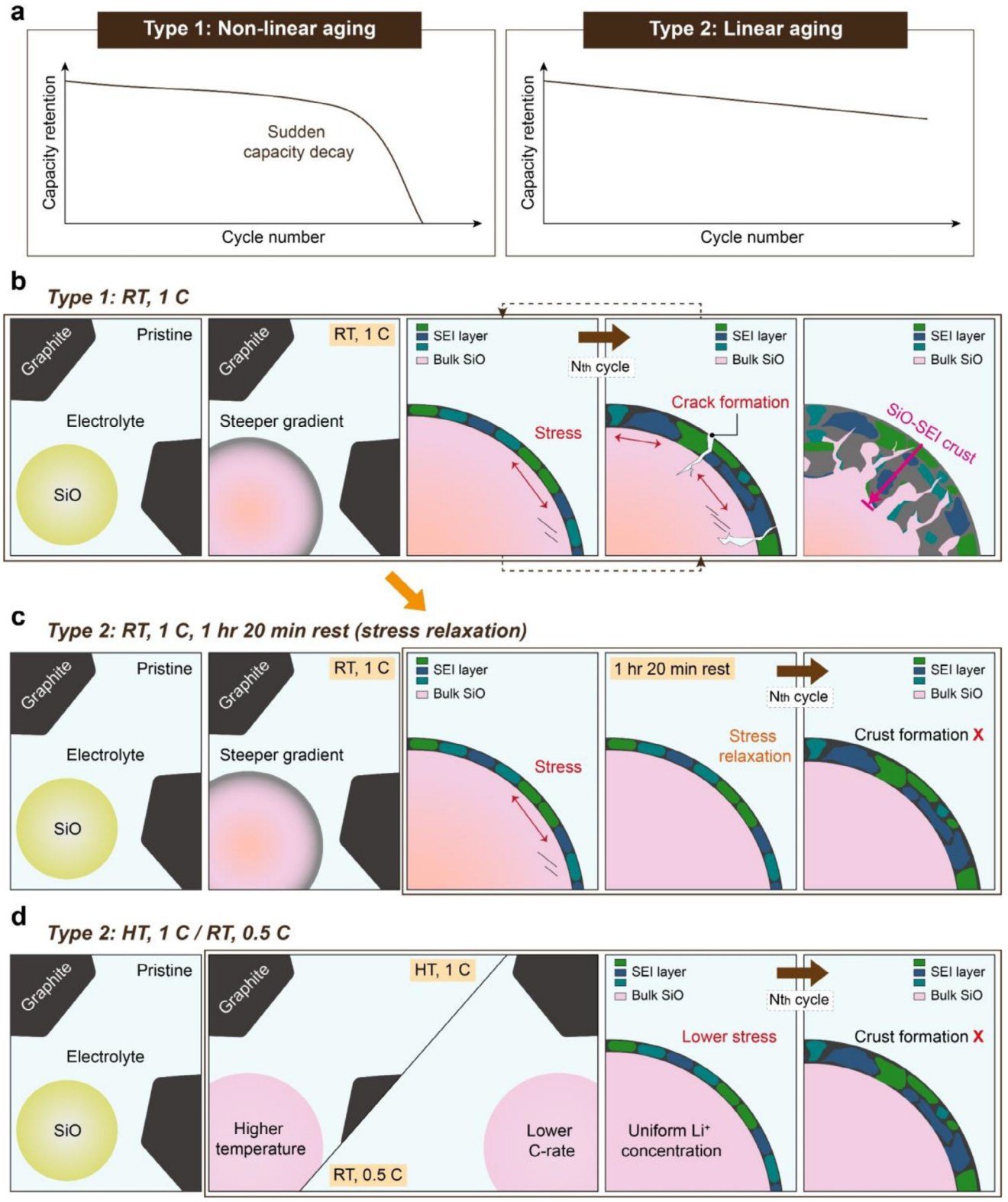

Figure 8. Schematic illustration of long-term cycling mechanisms of graphite/SiO anode. a) Type of aging in SiO-containing batteries. b–d) Transition of SiO particle in composite anode during repeated cycling b) under room temperature and 1 C (Type 1), c) under room temperature and 1 C with extended rest step, and d) under high temperature and 1 C or room temperature and 0.5 C.

surface. Similarly, at lower C-rates, the reduced lithium flux allows for more uniform Li^+ distribution, even though the diffusivity is slightly lower than at high temperatures. Both higher temperatures and lower C-rates effectively block the formation of the SiO-SEI crust and mitigate sudden capacity decay.

These findings are not limited to the specific SiO materials used in this study. Additional experiments using other silicon-based anodes, including Si/C and carbon-coated Mg-doped SiO electrodes, demonstrated similar temperature-dependent degradation trends under identical full cell cycling conditions in Figure 1c,d (see Figures S30 and S31, Supporting Information). Despite differences in composition and structure, these materials also exhibited severe damage at RT and stable morphology at HT, suggesting that the stress-induced SiO-SEI crust formation and the resulting sudden capacity fade may be a more general degradation mechanism for other silicon-based anode materials.

3. Conclusion

We investigate the degradation mechanism of graphite/SiO full cells under room temperature during long-term cycling. Despite the merits of the graphite/SiO anode in increasing the energy density of LIBs, it exhibits sudden capacity decay only at relatively lower temperatures and higher C-rates. This phenomenon arises from elevated stress on SiO surface under conditions such as room temperature and 1 C cycling, compared to high temperature or low C-rate conditions. The sustained stress induces crack formation, leading to lithium consumption in the full cell and the development of an SiO-SEI crust, ultimately resulting in the sudden capacity decay. Moreover, the mitigation of rapid capacity loss by extending the rest step in each cycle further validates the stress-induced transition as the mechanism driving sudden capacity decay, as evidenced by simulations and experimental results. We propose a nonlinear aging mechanism driven by sustained stress during long-term cycling in the Si-based anode. The present study on long-term cycling aging in Si-based anode provides useful insights into strategies for achieving an acceptable lifespan and higher energy densities in LIBs.

4. Experimental Section

Electrode Preparation: Pre-fabricated graphite, graphite/SiO (graphite: SiO = 85:15 wt%), and $LiNi_{0.6}Mn_{0.2}Co_{0.2}O_2$ (NCM622) electrodes were provided by LG Energy Solution, Ltd. SiO_x powder (with $x \approx 0.95$) was synthesized by evaporation of Si and SiO_2 under vacuum. The resulting bulk SiO was then milled to obtain the SiO powder with a median particle size (d50) of 6 µm, followed by carbon coating using chemical vapor deposition (CVD), as described in previous research.[51,52] The graphite and graphite/SiO anodes contained carbon black and single-walled carbon nanotubes (SWCNTs) as conductive additives, with sodium carboxymethyl cellulose (CMC) and styrene butadiene rubber (SBR) serving as binders. The NCM622 cathode was composed of NCM622, carbon black, and polyvinylidene fluoride (PVDF) in a weight ratio of 96:2:2. The areal capacity of the cathode was 3.285 mAh cm^{-2}, and the mass loading of the anodes was adjusted to achieve an N/P ratio of 1.06–1.08. Cathodes were punched into 12.7 mm diameter discs, and anodes into 14 mm discs for coin cell assembly. These electrodes were primarily used for the experiments.

For additional full cell tests using other silicon-based materials, commercial Si/C powder (MTI Korea) and carbon-coated silicon monooxide/Magnesium composite material (referred to as carbon-coated Mg-doped SiO, TCI Chemicals) were employed. Si/C was used as the only active material, while the carbon-coated Mg-doped SiO was blended with graphite at a weight ratio of 85:15 (graphite:SiO). To fabricate these anodes, a slurry was prepared by mixing the active material, super P, CMC, and SBR in a weight ratio of 90:3:2.8:4.2 in deionized water using an agate mortar. The slurry was cast onto a Cu foil using a doctor blade and dried in a vacuum oven at 100 °C overnight. These anodes were also assembled into full cells using the same NCM622 cathode provided by LG Energy Solution, Ltd. For the binder type comparison, the only difference from the CMC/SBR-based electrode was the binder composition: the graphite/SiO anode was prepared with a weight ratio of 90:3:7 (active material:Super P:PAA), with 15 wt% SiO in the active material, using poly(acrylic acid) (PAA, average $M_v \approx 450\,000$, Sigma–Aldrich) as the binder, and processed in N-methyl-2-pyrrolidone (NMP) under otherwise identical conditions.

Electrochemical Measurements: CR2032 coin-type cells (Sinopro Co., Ltd.) were assembled in an Ar-filled glovebox for electrochemical testing. A polyethylene (PE) membrane was employed as the separator, while the electrolyte consisted of 1.0 M $LiPF_6$ in ethylene carbonate/ethyl methyl carbonate (EC/EMC, 3:7 vol%) with 1.5 wt% vinylene carbonate (VC) and 0.5 wt% 1,3-propane sultone (PS) additives (from LG energy solution, Ltd.). The amount of electrolyte used for the electrochemical test is fixed at 30 µL. Full cells utilized NCM622 as the cathode, while half cells used Li metal as the counter electrode. All cells were rested for over 12 h before being cycled using either the WBCS3000 battery test system (WonATech Co., Ltd.) or the BTS4000 system (Neware Co., Ltd.). Room temperature measurements were conducted at 25 °C, and high-temperature measurements at 50 °C. Basically, all electrochemical tests were conducted at room temperature unless otherwise specified with the HT notation.

In full cell experiments, cells were charged at a constant current (CC) of 0.2 C up to 4.25 V (vs Li^+/Li), followed by a constant voltage (CV) hold until the current dropped to 0.033 C. After a 20-min rest, cells were discharged to 2.5 V at 0.2 C. This process was repeated three times to form the initial SEI layer. After the pre-cycling step, the applied C-rates and operating temperatures are specified in the corresponding figure captions or figures, respectively.

Half-cell experiments were performed to evaluate the capacity of NCM cathodes and graphite/SiO anodes, as shown in Figure 2d,f. Full cells were first disassembled in an Ar-filled glovebox, and the electrodes were retrieved. To remove residual electrolyte, the electrodes were thoroughly washed multiple times with EMC. Each electrode was then reassembled in a half-cell configuration with Li metal as the counter electrode. For the graphite/SiO half cells, a CC discharge was conducted at 0.05 C to 10 mV, followed by a CV hold until the current decreased to 0.01 C. After a 20-min rest, the cells were charged to 1.5 V at 0.05 C in CC mode. For the NCM half cells, a CC charge was performed at 0.05 C up to 4.3 V, followed by a 20-min rest before discharging to 3 V at a 0.05 C in a CC mode. This cycling protocol was repeated twice at 25 °C to determine the capacity of electrode.

In GITT test, SiO electrodes were prepared by mixing SiO, Super P, CMC, and SBR in deionized water, followed by casting on Cu foil. After one activation cycle (0.1 C CC discharge to 10 mV followed by CV until 0.017 C, then charge to 1.5 V at 0.1 C), the GITT protocol was conducted at 0.05 C with a 20-min current pulse and 40-min rest period. The lithium diffusion coefficient (D_{Li+}) was estimated using the simplified equation:[53]

$$D = \frac{4}{\pi\tau}\left(\frac{m_B V_m}{M_B S}\right)^2 \left(\frac{\Delta E_s}{\Delta E_\tau}\right)^2 \quad (1)$$

here, τ is the duration of the applied galvanostatic pulse; $m_B$and M_B are the mass and molar weight of the active material. V_m is the molar volume; S is the surface area of the electrode. $\Delta E\tau$ and ΔEs represent the voltage change during the current pulse and the equilibrium voltage change during the rest period, respectively.

Material Characterization: The graphite and graphite/SiO full cells were cycled at a current of 1 C (equivalent to 3.285 mA cm^{-2}). After cycling, the cells were disassembled in an Ar-filled glovebox to retrieve the

electrodes, which were rinsed multiple times with EMC to remove any residual electrolyte.

Cross-sectional scanning electron microscopy (SEM) images, along with energy dispersive X-ray spectroscopy (EDS) elemental maps and line scan profiles, were acquired using a field emission SEM (FE-SEM, Regulus 8230, Hitachi, Ltd.) operating at 15 kV. Six elements (C, O, F, Si, P, S) were analyzed for relative atomic composition. Vertical cross-sections of the electrodes were prepared using an ion milling system (IMS, ArBlade 5000, Hitachi, Ltd.) under cryo-vacuum conditions to minimize ion-beam damage and transferred to the chamber without air exposure.

X-ray computed tomography (CT) was performed at the Pohang Accelerator Laboratory (PAL) on beamline 7C, with 3D image reconstruction carried out using Avizo software.

Dynamic secondary ion mass spectrometry (D-SIMS, IMS 7f-Auto, CAMECA Co., Ltd.) was operated at 15 keV with a Cs^+ ion gun and a beam current of 1 pA, to obtain elemental mapping images.

The Chemical State study of etch elements were performed High-Performance X-ray Photoelectron Spectroscopy:HP-XPS(BS101), K-ALPHA+, Thermo Fisher Scientific Inc.(UK)) using monochromated Al *Kα* X-ray source ($h\nu$ = 1486.6 eV, power = 12 kV, 72 W) at a spot size of 400 µm in diameter with charge compensation using two flood gun(low energy electron and Ar+ ion) at Yeongnam Regional Center of Korea Basic Science Institute (KBSI). The XPS spectra were processed and fitted using Thermo Avantage software, and the calibration of all spectra was done using the C 1s C–C binding energy peak of 284.6 eV.

Transmission electron microscopy (TEM) analysis (Titan 80–300, Thermofisher Inc.) was conducted, operating at 300 kV. Images were recorded by a 4k x 4k CCD (Oneview 1095, Gatan) camera. Scanning transmission electron microscopy (STEM) images were collected using a Cs-corrected TEM (Titan 80–300, Thermofisher Inc.) operated at 300 kV equipped with a Gatan Quantum 966 spectrometer. Sample particles were prepared using a focused ion beam (FIB, Ethos NX5000, Hitachi, Ltd.) operated at 5–30 kV.

Simulation and Modeling: To investigate the role of Li^+ transport diffusion kinetics within SiO particles during charging and discharging process, the finite element analysis was conducted by using COMSOL Multiphysics V6.2. A multiphysics simulation was employed to model the Li-ion concentration resulting from lithium diffusion within SiO particles and the associated volumetric expansion and stress by combining solid mechanics and transport of diluted species. The combination of these two physics enabled the simultaneous simulation of mechanical and chemical changes. The total strain tensor (ε_{ij}) of the SiO particle was expressed by the following equation:

$$\varepsilon_{ij} = \varepsilon_{ij}^{e} + \varepsilon_{ij}^{c} \tag{2}$$

where, ε_{ij}^{e} is the elastic strain tensor, and ε_{ij}^{c} is the compositional strain tensor.[54] The elastic strain tensor, ε_{ij}^{e}, was defined by the stress-strain relationship given as,

$$\varepsilon_{ij}^{e} = \frac{1}{E}\left[(1+\nu)\,\sigma_{ij} - \nu\sigma_{kk}\delta_{ij}\right] \tag{3}$$

where E is the elastic modulus of single SiO particle, ν is Poisson's ratio, σ_{ij} is the stress tensor, σ_{kk} is the trace of stress tensor, and δ_{ij} is the Kronecker delta.[55] The compositional strain tensor, which describes the volumetric change of SiO according to the Li^+ concentration, was expressed by the following equation:

$$\varepsilon_{ij}^{c} = \beta_{ij}\,(c - c_0) \tag{4}$$

where β_{ij} is the expansion coefficient, c represents the Li^+ concentration, and c_0 is the initial Li concentration of particle.[56]

The diffusion of Li^+ inside of the SiO particle was modeled by the mass conservation equation, represented by Fick's second law of diffusion.[57] The Li^+ diffusion inside of the particle was expressed by following equation:

$$\frac{\partial c}{\partial t} + \nabla \cdot J = 0 \tag{5}$$

where J is the Li^+ flux through the SiO particle surface. The Li^+ flux was defined by Fick's first law of diffusion,

$$J = -D\nabla c \tag{6}$$

where D is the Li^+ diffusivity of SiO particle, which is impacted by the cell operation condition. To confirm the concentration and stress changes within SiO particle caused by different diffusion coefficients of SiO, the diffusion coefficients were set to $D_1 = 10^{-}11^{.5}$ cm^2 s^{-1}, $D_2 = 10^{-}11$ cm^2 s^{-1}, and $D_3 = 10^{-}1^{0.5}$ cm^2 s^{-1}, respectively. In addition, the electrochemistry modeling with the graphite/SiO electrode was performed under half-cell conditions. The current density vector (i_s) which flows through the electrode cross-sectional area is proportional to the electric field ($\nabla\phi_s$) and calculated by Ohm's law as following equation:[58]

$$i_s = -\sigma_s \nabla \phi_s \tag{7}$$

where σ_s and ϕ_s represent the intrinsic electrical conductivity and electric potential value of an active materials. The charged Li^+ transfer behavior (i_l) in the liquid electrolyte region was modeled by the following equation:

$$i_l = -\sigma_l \nabla \phi_l + \frac{2\sigma_l RT}{F}\left(1 + \frac{\partial lnf}{\partial lnc_l}\right)\left(1 - t_+\right)\nabla lnc_l \tag{8}$$

where σ_l, ϕ_l, F, R, f, c_l, and t_+ represent the ionic conductivity of the liquid electrolyte, electrolyte potential, Faraday constant, universal gas constant, molar activity coefficient, electrolyte concentration, and transport number, respectively.

Li-ion mass transport in the liquid electrolyte was modeled by Fick's second law of diffusion:

$$\frac{\partial c_l}{\partial t} = \nabla \cdot (D_l \nabla c_l) - \frac{i_l t_+}{F} \tag{9}$$

where D_l represents the Li^+ diffusion coefficient of liquid electrolyte.

The local current density (i) which attributed to the charge transport of Li^+ at the electrode–electrolyte interface was expressed by following equation:

$$i = i_0\left(\exp\left(\frac{(1-\alpha)\,F\eta}{RT}\right) - exp\left(\frac{\alpha F\eta}{RT}\right)\right) \tag{10}$$

where i, α, η, and i_0 represent the local current density at the electrode and electrolyte interface.[59]

Supporting Information

Supporting Information is available from the Wiley Online Library or from the author.

Acknowledgements

This work was supported by the National Research Foundation of Korea (NRF) grant funded by the Korea government (MSIT) (RS-2024-00422387) and by LG Energy Solution. Y.J.C acknowledges the support by Basic Science Research Program through the National Research Foundation of Korea (NRF) funded by the Ministry of Education (RS-2024-00415596). J.S.B. acknowledges support by the Ministry of Science and ICT in Korea via KBSI (Grant No. C524100). Y.K. acknowledges the support by Basic Science Research Program through the National Research Foundation of Korea (NRF) funded by the Ministry of Education (RS-2024-00453388).

Conflict of Interest

The authors declare no conflict of interest.

Author Contributions

Y.J.C., J.-Y.B., and S.P. contributed equally to this work. S.-H.Y. and J.M. conceived the concept and supervised the project. Y.J.C. and J.-Y.B. designed and planned the main experiments. Y.J.C. and J.-Y.B. conducted electrochemical measurements and characterizations. S.P. performed computational calculations under the supervision of J.M. Y.K. and B.M.W. conducted processing of the CT data. S.H.K. and H.K. performed cross-sectional SEM experiments. T. K., S.Y.S. and Y.L. provided the cell components and participated in the scientific discussion. Y.J.C. and J.-Y.B. prepared the manuscript. All authors have confirmed the final version of the manuscript.

Data Availability Statement

The data that support the findings of this study are available from the corresponding author upon reasonable request.

Keywords

diffusion-induced stress, graphite/SiO anodes, lithium-ion batteries, long-term cycling, sudden capacity decay

Received: April 16, 2025
Revised: August 12, 2025
Published online:

[1] Y. Ding, Z. P. Cano, A. Yu, J. Lu, Z. Chen, *Electrochem. Energy Rev.* **2019**, *2*, 1.
[2] J. Liu, J. Xiao, J. Yang, W. Wang, Y. Shao, P. Liu, M. S. Whittingham, *Next Energy* **2023**, *1*, 100015.
[3] C. Xu, Q. Dai, L. Gaines, M. Hu, A. Tukker, B. Steubing, *Commun. Mater.* **2020**, *1*, 99.
[4] F. Degen, M. Winter, D. Bendig, J. Tübke, *Nat. Energy* **2023**, *8*, 1284.
[5] M. Li, J. Lu, Z. Chen, K. Amine, *Adv. Mater.* **2018**, *30*, 1800561.
[6] N. Nitta, F. Wu, J. T. Lee, G. Yushin, *Mater. Today* **2015**, *18*, 252.
[7] B. A. Boukamp, G. C. Lesh, R. A. Huggins, *J. Electrochem. Soc.* **1981**, *128*, 725.
[8] H. Wu, Y. Cui, *Nano Today* **2012**, *7*, 414.
[9] J. W. Choi, D. Aurbach, *Nat. Rev. Mater.* **2016**, *1*, 16013.
[10] J. H. Ryu, J. W. Kim, Y.-E. Sung, S. M. Oh, *Electrochem. Solid-State Lett.* **2004**, *7*, A306.
[11] F. Shi, Z. Song, P. N. Ross, G. A. Somorjai, R. O. Ritchie, K. Komvopoulos, *Nat. Commun.* **2016**, *7*, 11886.
[12] N. Kim, Y. Kim, J. Sung, J. Cho, *Nat. Energy* **2023**, *8*, 921.
[13] G. G. Eshetu, H. Zhang, X. Judez, H. Adenusi, M. Armand, S. Passerini, E. Figgemeier, *Nat. Commun.* **2021**, *12*, 5459.
[14] M. Ashuri, Q. He, L. L. Shaw, *J. Power Sources* **2023**, *559*, 232660.
[15] M. Choi, E. Lee, J. Sung, N. Kim, M. Ko, *Nano Res.* **2024**, *17*, 5270.
[16] S. C. Jung, H.-J. Kim, J.-H. Kim, Y.-K. Han, *J. Phys. Chem. C* **2016**, *120*, 886.
[17] Y. Li, X. Zheng, Z. Cao, Y. Wang, Y. Wang, L. Lv, W. Huang, Y. Huang, H. Zheng, *Energy Storage Mater.* **2023**, *55*, 660.
[18] A. Bordes, E. D. Vito, C. Haon, A. Boulineau, A. Montani, P. Marcus, *Chem. Mater.* **2016**, *28*, 1566.
[19] L. Zhang, Y. Qin, Y. Liu, Q. Liu, Y. Ren, A. N. Jansen, W. Lu, *J. Electrochem. Soc.* **2018**, *165*, A2102.
[20] Y. He, L. Jiang, T. Chen, Y. Xu, H. Jia, R. Yi, D. Xue, M. Song, A. Genc, C. Bouchet-Marquis, *Nat. Nanotechnol.* **2021**, *16*, 1113.
[21] S. Park, J. Sung, S. Chae, J. Hong, T. Lee, Y. Lee, H. Cha, S. Y. Kim, J. Cho, *ACS Nano* **2020**, *14*, 11548.
[22] J. Guo, D. Dong, J. Wang, D. Liu, X. Yu, Y. Zheng, Z. Wen, W. Lei, Y. Deng, J. Wang, G. Hong, H. Shao, *Adv. Funct. Mater.* **2021**, *31*, 2102546.
[23] C. E. L. Foss, A. M. Svensson, Ø. Gullbrekken, S. Sunde, F. Vullum-Bruer, *J. Energy Storage* **2018**, *17*, 395.
[24] M.-T. F. Rodrigues, G. Babu, H. Gullapalli, K. Kalaga, F. N. Sayed, K. Kato, J. Joyner, P. M. Ajayan, *Nat. Energy* **2017**, *2*, 17108.
[25] X. Liu, L. Yin, D. Ren, L. Wang, Y. Ren, W. Xu, S. Lapidus, H. Wang, X. He, Z. Chen, G.-L. Xu, M. Ouyang, K. Amine, *Nat. Commun.* **2021**, *12*, 4235.
[26] M. Simolka, J.-F. Heger, H. Kaess, I. Biswas, K. A. Friedrich, *J. Appl. Electrochem.* **2020**, *50*, 1101.
[27] K. Jalkanen, J. Karppinen, L. Skogström, T. Laurila, M. Nisula, K. Vuorilehto, *Appl. Energy* **2015**, *154*, 160.
[28] S. S. Zhang, K. Xu, T. R. Jow, *Electrochim. Acta* **2002**, *48*, 241.
[29] J. Hou, M. Yang, D. Wang, J. Zhang, *Adv. Energy Mater.* **2020**, *10*, 1904152.
[30] A. Gupta, A. Manthiram, *Adv. Energy Mater.* **2020**, *10*, 2001972.
[31] S. Ma, M. Jiang, P. Tao, C. Song, J. Wu, J. Wang, T. Deng, W. Shang, *Prog. Nat. Sci.: Mater. Int.* **2018**, *28*, 653.
[32] Y. Feng, L. Zhou, H. Ma, Z. Wu, Q. Zhao, H. Li, K. Zhang, J. Chen, *Energy Environ. Sci.* **2022**, *15*, 1711.
[33] J. Wang, Q. Zheng, M. Fang, S. Ko, Y. Yamada, A. Yamada, *Adv. Sci.* **2021**, *8*, 2101646.
[34] S. M. Rezvanizaniani, Z. Liu, Y. Chen, J. Lee, *J. Power Sources* **2014**, *256*, 110.
[35] J. D. McBrayer, M.-T. F. Rodrigues, M. C. Schulze, D. P. Abraham, C. A. Apblett, I. Bloom, G. M. Carroll, A. M. Colclasure, C. Fang, K. L. Harrison, G. Liu, S. D. Minteer, N. R. Neale, G. M. Veith, C. S. Johnson, J. T. Vaughey, A. K. Burrel, B. Cunningham, *Nat. Energy* **2021**, *6*, 866.
[36] B. S. Lee, S.-H. Oh, Y. J. Choi, M.-J. Yi, S. H. Kim, S.-Y. Kim, Y.-E. Sung, S. Y. Shin, Y. Lee, S.-H. Yu, *Nat. Commun.* **2023**, *14*, 150.
[37] P. M. Attia, A. Bills, F. B. Planella, P. Dechent, G. d. Reis, M. Dubarry, P. Gasper, R. Gilchrist, S. Greenbank, D. Howey, *J. Electrochem. Soc.* **2022**, *169*, 060517.
[38] A. Barai, K. Uddin, W. D. Widanage, A. McGordon, P. Jennings, *Sci. Rep.* **2018**, *8*, 21.
[39] S. Barcellona, S. Colnago, G. Dotelli, S. Latorrata, L. Piegari, *J. Energy Storage* **2022**, *50*, 104658.
[40] H. Villarraga-Gómeza, D. L. Beguna, P. Bhattada, K. Mo, M. N. Radc, R. T. White, S. T. Kelly, *Nondestruct. Test. Eval.* **2022**, *37*, 519.
[41] C. Cao, I. I. Abate, E. Sivonxay, B. Shyam, C. Jia, B. Moritz, T. P. Devereaux, K. A. Persson, H.-G. Steinrück, M. F. Toney, *Joule* **2019**, *3*, 762.
[42] H. Takezawa, S. Ito, H. Yoshizawa, T. Abe, *Electrochim. Acta* **2017**, *229*, 438.
[43] D. Rehnlund, F. Lindgren, S. Böhme, T. Nordh, Y. Zou, J. Pettersson, U. Bexell, M. Boman, K. Edström, L. Nyholm, *Energy Environ. Sci.* **2017**, *10*, 1350.
[44] B.-C. Yu, Y. Hwa, C.-M. Park, H.-J. Sohn, *J. Mater. Chem. A* **2013**, *1*, 4820.
[45] J. Han, S. Jo, I. Na, S. Oh, Y. Jeon, Y. Park, B. Koo, H. Hyun, S. Seo, D. Lee, H. Kim, J. Kim, J. Lim, J. Lim, *ACS Appl. Mater. Interfaces* **2021**, *13*, 52202.
[46] J. Lin, L. Wang, Q. Xie, Q. Luo, D.-L. Peng, C. B. Mullins, A. Heller, *Angew. Chem., Int. Ed.* **2023**, *62*, 202216557.
[47] J. D. McBrayer, C. A. Apblett, K. L. Harrison, K. R. Fenton, S. D. Minteer, *Nanotechnology* **2021**, *32*, 502005.

[48] L. W. Sommer, P. Kiesel, A. Ganguli, A. Lochbaum, B. Saha, J. Schwartz, C.-J. Bae, M. Alamgir, A. Raghavan, *J. Power Sources* **2015**, *296*, 46.
[49] X. Zhu, Y. Chen, H. Chen, W. Luan, *Int. J. Mech. Sci.* **2020**, *178*, 105608.
[50] C.-F. Chen, P. Barai, P. P. Mukherjee, *J. Electrochem. Soc.* **2014**, *161*, A2138.
[51] T. Hirose, M. Morishita, H. Yoshitake, T. Sakai, *Solid State Ionics* **2017**, *303*, 154.
[52] I. Choi, M. J. Lee, S. M. Oh, J. J. Kim, *Electrochim. Acta.* **2012**, *85*, 369.
[53] K. Pan, F. Zou, M. Canova, Y. Zhu, J.-H. Kim, *J. Power Sources* **2019**, *413*, 20.
[54] Y. Gwak, J. Moon, M. Cho, *J. Power Sources* **2016**, *307*, 856.
[55] X. Zhang, W. Shyy, A. M. Sastry, *J. Electrochem. Soc.* **2007**, *154*, A910.
[56] S. Lou, Q. Liu, F. Zhang, Q. Liu, Z. Yu, T. Mu, Y. Zhao, J. Borovilas, Y. Chen, M. Ge, X. Xiao, W.-K. Lee, G. Yin, Y. Yang, X. Sun, J. Wang, *Nat. Commun.* **2020**, *11*, 5700.
[57] J. Moon, J. Y. Jung, T. D. Hoang, D. Y. Rhee, H. B. Lee, M.-S. Park, J.-S. Yu, *J. Power Sources* **2021**, *486*, 229359.
[58] J. Moon, T. D. Hoang, S. S. Park, S. Park, D. Y. Rhee, J. Lee, S. A. Han, M.-S. Park, J. H. Kim, *J. Energy Chem.* **2022**, *71*, 470.
[59] D. W. Kang, S. S. Park, H. J. Choi, J.-H. Park, J. H. Lee, S.-M. Lee, J.-H. Choi, J. Moon, B. G. Kim, *ACS Nano* **2022**, *16*, 11892.